Comparative Analysis of Active Impedance Matching Interfaces for Piezoelectric Energy Harvesters

Amanda Vanderwegen[1] · Rodrigo W. Porto[1] · Lucas Murliky[1] · Ivan Müller[1] · Fernando R. de Sousa[2] ·
Valner J. Brusamarello[1]

Abstract

This paper conducts a comparative study of the output energy generated by two compensation approaches for piezoelectric energy harvesters. These transducers are typically coupled to a cantilevered beam, and the compensation circuitry enhances the harvester's performance under an input mechanical vibration stimulus. The output power of the piezoelectric transducer relies on both the reflected and intrinsic mechanical impedance, along with the total output load. The electrical equivalent circuit of the structure, incorporating the transducer, is primarily capacitive, leading to an out-of-phase relationship between current and voltage in the electrical domain, resulting in the generation of reactive power and a subsequent reduction in the overall system efficiency. The system's first vibration mode, corresponding to a very low frequency, requires a significant passive inductor for impedance matching to ensure maximum power transfer to the load. In the first approach, a non-Foster circuit is implemented as a reactance for impedance matching, employing a Negative Impedance Converter (NIC) circuit. In another approach, the output of the cantilever beam is assessed using a synchronized switched inductor (SSHI). Both approaches are examined, and their feasibility limits are evaluated, taking into account the energy balance generated by the piezoelectric transducer. Experimental results illustrate that the active matching approach with a non-Foster reactance shows a greater enhancement in energy compared to the SSHI compensation method under conditions of harmonic mechanical oscillations.

Keywords Energy harvesting · Piezoelectricity · Impedance matching · Non-Foster impedance

1 Introduction

Energy harvesting (EH) is the process of extracting usable energy from natural and human-made sources that surround our everyday environment (Pradeesh et al., 2022). Various techniques have been proposed to capture energy from diverse sources, including mechanical vibration, solar, thermal, etc (Batra et al., 2018; Cesarini et al., 2017; Naifar et al., 2017). The availability of renewable energy enables the application of the concept of green energy to low-power devices such as wireless autonomous sensor nodes. Typically, these devices have limited battery capacity, which compromises their lifespan, processing capacity, and operating range (Lallart et al., 2012; Ruan et al., 2017). This concept is also applied in other areas, including health and lifestyle equipment (Fan et al., 2024; Roy et al., 2022; Kalantarian & Sarrafzadeh, 2016; Kuang et al., 2017; Bao et al., 2021), remote vibration sensors (Kraśny & Bowen, 2021), vehicles (Pan et al., 2017; Qi et al., 2022), intelligent buildings (Bao & Tang, 2017), among others (Xu et al., 2018; Varoto, 2015).

Piezoelectric energy harvesters (PEH) are transducers used for electric power generation from mechanical motion or vibration and the piezoelectricity is based on the property of some materials that are capable to convert a mechanical stimulus into electrical energy (Liang & Liao, 2011; Khoo et al., 2017; Pradeesh et al., 2022) or an electrical stimulus to

Amanda Vanderwegen, Rodrigo W. Porto, Lucas Murliky, Ivan Müller, Fernando R. de Sousa and Valner J. Brusamarello have contributed equally to this work.

✉ Valner J. Brusamarello
brusamarello.valner@gmail.com

1 PPGEE, Universidade Federal do Rio Grande do Sul, Oswaldo Aranha. 99. S. 701, Porto Alegre 90035-190, RS, Brazil

2 Electric and Electronics Department, Universidade Federal de Santa Catarina, Reitor João David Ferreira Lima, s/no, Trindade, Florianópolis 88040-900, SC, Brazil

a mechanical movement. Usually, piezoelectric transducers are coupled to a cantilevered beam. Thus, the response of the whole system is dependent on the mechanical features, the connected electrical circuit and the load (Liang & Liao, 2010).

Various optimization techniques have been employed for piezoelectric transducers. For example, Peng et al. (2019) introduced an interface circuit designed to hold a constant voltage at the load, irrespective of vibration intensity, thereby enhancing the efficiency of the piezoelectric generator beyond its resonant frequency. Additionally, in Deepak and George (2021), the authors devised a system incorporating permanent magnets coupled to both the piezoelectric beam and the structure experiencing vibrations. This arrangement leverages the repulsive force between the magnets to amplify the oscillatory movement of the beam, thereby improving the overall performance of the energy collector.

Synchronized switch harvesting on inductor (SSHI) is a technique that involves connecting a non-resonant inductance, resulting in a significant enhancement of the energy collector's performance (Guyomar et al., 2005; Bradai et al., 2021). The reported efficiency improvements for the harvesting system with P-SSHI and S-SSHI techniques are approximately 500% and 400%, respectively, compared to a regular circuit (Chao, 2011; Liang & Liao, 2012a). These techniques enable operation across a broad frequency range; however, they require zero-crossing detection and switching synchronization to avoid phase delays (Lallart et al., 2012).

By replacing the inductance with a transformer, a variation of the SSHI technique is introduced, known as "SSHI-MR" (synchronized switch harvesting on inductor using magnetic rectifier). This variant is suitable for capturing energy at low output voltage levels and requires two switches (Garbuio et al., 2009). Another variation of SSHI, termed SSDCI (synchronized switching and discharging to a storage capacitor through an inductor), involves transferring energy from the piezoelectric energy harvester (PEH) to a storage capacitor through an inductance (Wu et al., 2009). Several other variations of the SSHI technique exist, including an active energy harvesting scheme (Liu et al., 2009), a technique called SECE (synchronous electric charge extraction) designed to make energy generation independent of the load (Lefeuvre et al., 2005), and combinations of these techniques such as DSSH (double synchronized switch harvesting) (Lallart et al., 2008) and ESSH (enhanced synchronized switch harvesting) (Shen et al., 2010). All these techniques share the commonality of having one or more switches connecting or disconnecting electrical circuit elements.

Another technique for enhancing the performance of the energy harvester, particularly when dealing with harmonically mechanical oscillations, involves connecting a resonant inductance to compensate for the equivalent intrinsic capacitive impedance of the PEH (Priya, 2007; Liang & Liao, 2011;

Brufau-Penella & Puig-Vidal, 2009; Giuliano & Zhu, 2014). This tuning of the circuit helps mitigate the degrading effect of internal impedance. However, as natural mechanical vibrations often concentrate most of their energy on low-frequency components, the compensating inductance value can become impractically large, reaching magnitudes on the order of kH (Lossouarn et al., 2017; Giuliano & Zhu, 2014). The use of such a passive element becomes impractical. Therefore, a more viable solution is the implementation of reactive elements with active devices, such as generalized impedance converters (GIC) or negative impedance converters (NIC) (Franco, 2002). Both NIC and GIC can be implemented in a compact form and require energy to supply the active devices. Strictly speaking, GIC circuits adhere to the Foster Theorem, despite the use of active devices (Foster, 1924), while NIC circuits implement negative reactances and clearly do not adhere to the Foster Theorem.

Both of the techniques presented (SSHI or the active matching approach—AMA) need to be self-powered, either to provide drive circuits for the electronic switches or to supply the operational amplifiers implementing active elements. Consequently, the energy gain achieved with the compensation technique must exceed the energy consumed by the components added to the circuit. In this study, we analyze the details of the presented techniques considering a Piezoelectric energy harvester (PEH) coupled to an aluminum cantilever beam operating under a mechanical stimulus exciting the fundamental mode of vibration. We compare the performance of both methods with the PEH circuit connected to a resistive load without any form of compensation. Figure 1 illustrates the equivalent circuit of the PEH connected to the interface matching circuit and the load. The primary contribution of this work is to showcase the advantages and disadvantages of both techniques, along with an analysis of the total balance of electrical power transferred to the load under the same input conditions. The technical viability of employing the AMA technique has been extensively demonstrated in Porto et al. (2023), with certain findings reiterated alongside the implementation of the NIC. While the primary focus of Porto et al. (2023) was to establish the method's feasibility, the present article not only contextualizes the application of harvesting but also evaluates its performance in light of a well-defined mechanical stimulus applied to the cantilever beam with SSHI.

2 Piezoelectric Energy Harvester

Piezoelectricity is defined as the property exhibited by certain dielectric materials to generate mechanical deformation when subjected to an electric field. Conversely, when these piezoelectric materials undergo mechanical deformation, they produce electrical polarization. In both instances, there
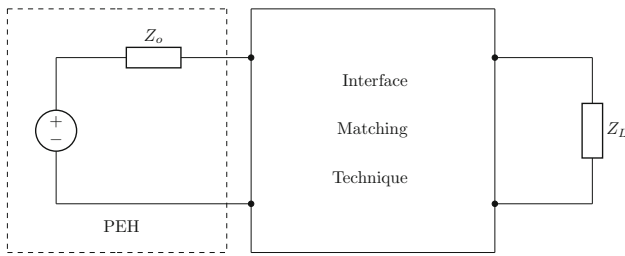
Fig. 1 PEH connected to an interface matching circuit for optimizing the overall performance, where Z_o is the equivalent output impedance of the PEH and Z_L the load
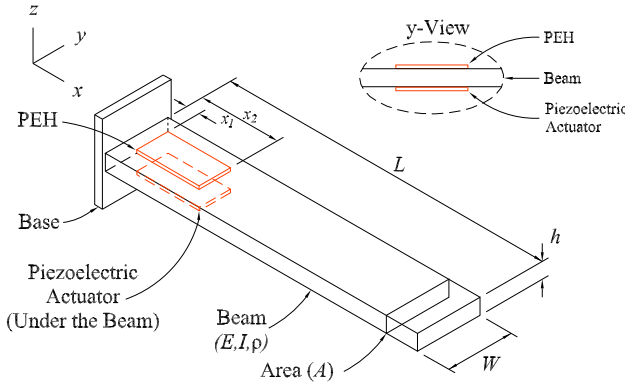

Fig. 2 Euler–Bernoulli beam with piezoelectric pair

is a conversion of energy (IEEE, 1988). The piezoelectric energy harvester (PEH) is typically affixed to a cantilever beam (as depicted in Fig. 2), which determines the dynamic mechanical characteristics of the system. Additionally, the transformed electrical energy collected is described by the Euler-Bernoulli equations (Moheimani & Fleming, 2006; Halim & Moheimani, 2001). Assuming the most of the output energy is concentrated in a finite number M of harmonic components, the natural vibration frequency of such a cantilever beam can be approximated by Moheimani and Fleming (2006); Henrion et al. (2004):

$$f_n = \frac{\omega_n}{2\pi} = \frac{1}{2\pi} \frac{EI}{\rho A} \beta^2 \tag{1}$$

where I is the moment of inertia of the beam, A is the cross-sectional area, ρ is the bulk density and E is the beam Young's constant.

The values of β are found numerically by:

$$cos(\beta L)cosh(\beta L) = -1. \tag{2}$$

It is important to note that (2) has infinite solutions, each corresponding to the infinite modes of system vibrations. Understanding the natural vibration modes or frequencies of the system is crucial for optimizing the energy generation of the harvester.

2.1 Equivalent Electromechanical Circuit Model

The cantilever beam can be simplified by a vibrating structure model, with one degree of freedom. The lumped electro mechanical model is composed of a moving mass M, a spring representing the stiffness of the piezoelectric element K and the damping D. The mass M moves with a displacement $u(t)$ in the z direction (Fig. 2) due to an external vibration $y(t)$.

Thus, the cantilever beam with the coupled PEH can be represented by the equivalent circuit of Fig. 3 (Erturk & Inman, 2008; Chao, 2011). The equations coupling both mechanical and electrical domain can be represented by Badel et al. (2006); Xia et al. (2018); Huang and Hsieh (2021); Arroyo et al. (2012); Guyomar et al. (2005); Lefeuvre et al. (2005); Liu et al. (2009):

$$M\ddot{u} + D\dot{u} + Ku + \alpha V_P = F_m \tag{3}$$
$$i_P = \alpha\dot{u} - C_P \dot{V}_P \tag{4}$$

where, M, D, K, α and C_P are the modal mass, damping coefficient, equivalent stiffness, piezoelectric force-voltage factor and piezoelectric clamped capacitance, respectively. Furthermore, F_m and $\dot{u}$ are the input mechanical vibrating force and velocity in the mechanical domain; V_P and i_P are the output piezoelectric voltage and current in the electrical domain.

The piezoelectric force-voltage factor α represents the capability of the piezoelectric material to convert mechanical energy into electrical energy (Arroyo et al., 2012; Moheimani & Fleming, 2006). In Fig. 3, the equivalent electric circuit of both mechanical and electrical domains is depicted, neglecting intrinsic losses. The mechanical domain elements can be translated to the electrical domain using the factor α. Therefore, we define the reflected mechanical impedance in the Laplace domain as:

$$Z_m(s) = \frac{D}{\alpha^2} + M\frac{s}{\alpha^2} + \frac{K}{s\alpha^2} \tag{5}$$

This is an equivalent R, L and C second order circuit, where the damping factor represents the resistance $R = \frac{D}{\alpha^2}$, the mass represents the inductance $L = \frac{M}{\alpha^2}$ and the effective stiffness the capacitance $C = \frac{\alpha^2}{K}$. The current and voltage sources in the electrical domain can be defined (Fig. 4):

$$I_{eq}(s) = s\alpha u + \frac{V_P(s)}{Z_m(s)} \tag{6}$$
$$V_{eq}(s) = s\alpha u Z_m(s) + V_P(s) \tag{7}$$

Figure 4 shows the simplified equivalent circuits with the reflected mechanical impedance Z_m and the equivalent capacitance C_P.

Fig. 3 Both mechanical and electrical domains of the PEH equivalent electrical circuit
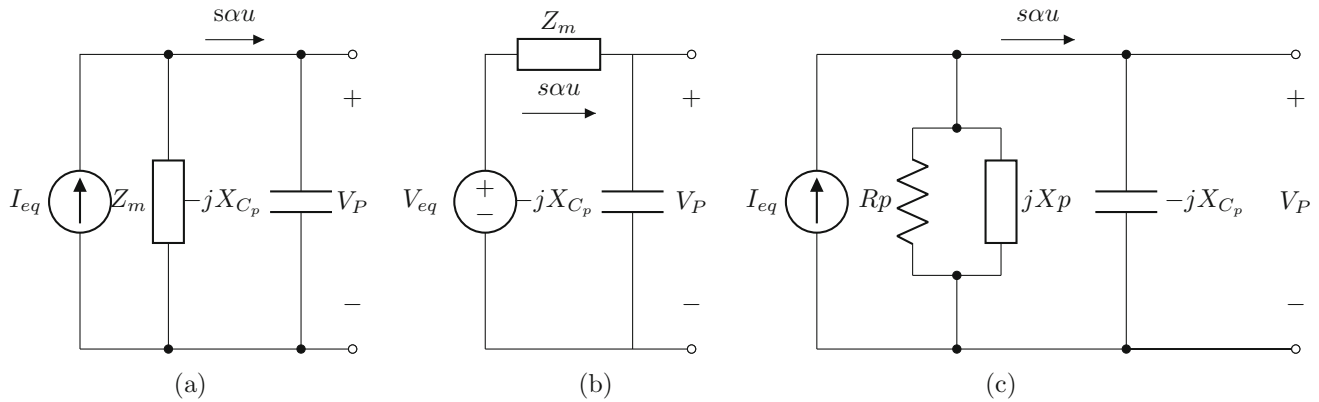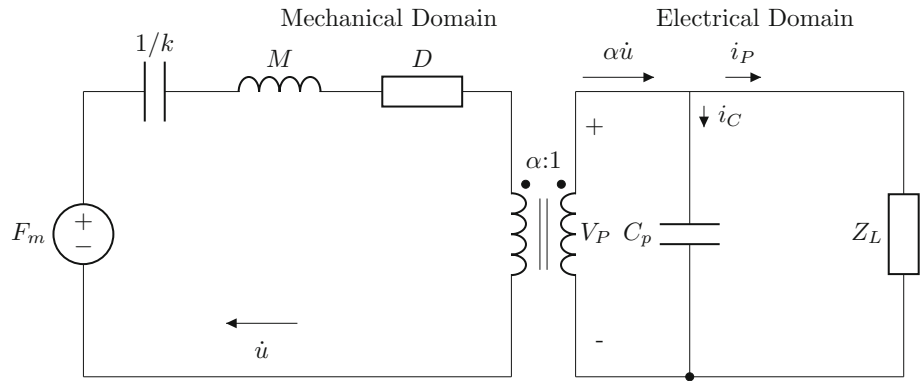

Fig. 4 PEH simplified electrical equivalent circuit: **a** Norton equivalent circuit; **b** Thèvenin equivalent circuit; and **c** Norton equivalent circuit with Z_m decomposed in parallel equivalent resistance and reactance

In most energy harvesting applications, the connection to the load involves a rectifier, as depicted in Fig. 5. For simplicity, we can assume that the capacitor of the rectifier, denoted as C_r, is large enough to ensure a constant voltage $V_c(t)$ across the load (Shu & Lien, 2006). Additionally, in harmonically excited cases (such as the cantilevered beam), the rectifier can be approximated with an equivalent resistance $R_{eq} = \frac{8}{\pi^2} R_L$ (Liang & Liao, 2012b; Steigerwald, 1988), as shown in Fig. 5b.

The simplified circuit in Fig. 5 reveals that the impedance Z_m in conjunction with the impedance imposed by C_P induces a phase shift between the voltage V_P and the equivalent current I_{eq}, consequently degrading the power delivered to the load. The total equivalent impedance seen from the source, denoted as Z_T, can be calculated as follows:

$$
\begin{aligned}
Z_T(j\omega) &= \frac{1}{\frac{1}{Z_m} + j\omega C_P} = \frac{1}{Y_T(j\omega)} \\
&= Z_{T_{Re}} + Z_{T_{Im}} = |Z_T| \angle \Phi_Z
\end{aligned}
\tag{8}
$$

Hence, different methods can be employed to match the circuit and load impedances for maximizing delivered power. In fact, rather than aiming for impedance matching, simply minimizing Φ_Z could significantly enhance the performance

of the PEH. This article explores two approaches for minimizing the reactive portion of the intrinsic impedance.

2.2 Compensation Methods for Synchronizing the PEH Circuit

Two methods to minimize Φ_Z are presented:

i. The Active Matching Approach (AMA) suggests inserting a reactive element in the PEH equivalent circuit, emulated by an active device.
ii. The Synchronized Switch Harvesting on Inductor (SSHI) method proposes inserting a switched passive inductor during a short time interval.

2.2.1 AMA

This approach aims to eliminate the reactive component, minimizing the phase angle between voltage and current at the output of the PEH. Maximum power transfer occurs when the load matches the conjugate of the internal impedance of the source delivering energy to the circuit (Alexander & Sadiku,

2013; Giuliano & Zhu, 2014):

$$Z^{match} = Z_T^* = Z_{T_{Re}} - Z_{T_{Im}} = |Z_T| \angle - \Phi_Z \qquad (9)$$

From Fig. 4(c) one can express the parallel form of the reflected mechanical impedance Z_m in terms of the admittance by:

$$Y_m = \frac{1}{R_p} - j\frac{1}{X_p} = \frac{1}{R_s + jX_s} \qquad (10)$$

where $R_s = R$ and $X_s = j\omega L - j\frac{1}{\omega C}$ are the real and imaginary part of Z_m, respectively, in the series form expressed in (5). Thus, (10) can be solved for R_p and X_p by equating its real and imaginary parts:

$$\begin{cases} R_p = R_s(1 + Q^2) \\ X_p = X_s(1 + \frac{1}{Q^2}) \end{cases} \qquad (11)$$

where $Q = \frac{X_s}{R_s}$ is the quality factor of the RLC series form.

The parallel form of the reflected mechanical impedance Z_m is useful to calculate the total impedance seen at the PEH's terminals. The imaginary part X_p can be associated with X_{C_p} and the compensation inductance, L_{comp}, is determined in order to eliminate the imaginary part of Z_T:

$$L_{comp} = \frac{1}{\omega}\left[\frac{X_p X_{C_p}}{X_p - X_{C_p}}\right] \qquad (12)$$

where, $X_{C_p} = \frac{1}{\omega C_p}$.

Because L_{comp} is too high, this component is implemented with an active circuit. The use of an active circuit in this application only makes sense if the energy balance is positive; in other words, the energy consumption of the active circuit should be less than the total energy gain generated in the load with the tuned PEH.

According to Foster's theorem (Foster, 1924), passive elements always have the derivative of the reactance function in relation to the angular frequency positive. Alternatively, networks that do not adhere to Foster's theorem can be synthesized with the help of carefully designed active circuits. An advantage of these circuits is the ability to adjust the reactance value, allowing for variable impedance matching or even implementing very high reactances in a small volume. Such behavior can be advantageous for matching the impedances of the PEH over a broad frequency range. A typical class of such circuits is called NIC, which is based on operational amplifiers with both positive and negative feedback.
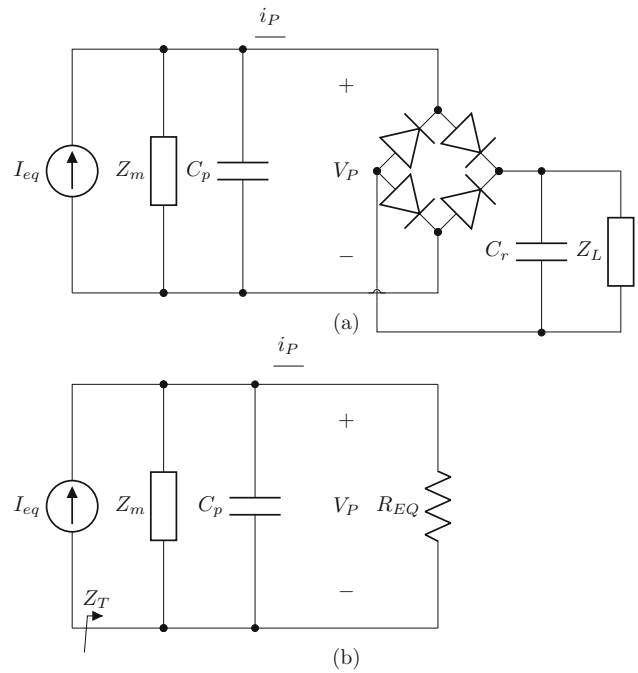

Fig. 5 Euler–Bernoulli PEH equivalent electrical circuit with explicit diode bridge; **b** simplified PEH and rectifier equivalent circuit

A typical implementation of a NIC is depicted in Fig. 6. Considering the ideal model of the operational amplifier, the input impedance Z_{NIC} seen from the terminals a and b is given by:

$$Z_{NIC} = -\frac{R_1}{R_2} \cdot Z_R \qquad (13)$$

where Z_R is a reference impedance.

To match the output impedance of the PEH, $Z_T(j\omega)$, one should connect the NIC circuit (Fig. 6a) at the V_P terminals, as shown in Fig. 6b. By using a capacitor (C_r) as the reference impedance for the NIC circuit (Z_r), then its input impedance yields yields $Z_{NIC} = jX_N$.

Considering the total equivalent impedance of the PEH as the parallel connection of Z_m (presented in (11)), the piezoelectric capacitance C_P, and the input impedance of the NIC circuit given by (13), the total admittance $Y(j\omega)$ can be expressed as:

$$Y(j\omega) = \frac{1}{R_p} - j\frac{1}{X_p} + j\frac{1}{X_{C_p}} + \frac{1}{Z_{NIC}} \qquad (14)$$

Thus, in order to cancel the imaginary part of (14), the NIC impedance should be:

Fig. 6 **a** Negative impedance converter (NIC). **b** The equivalent circuit of the PEH attached to the cantilever beam with the NIC circuit
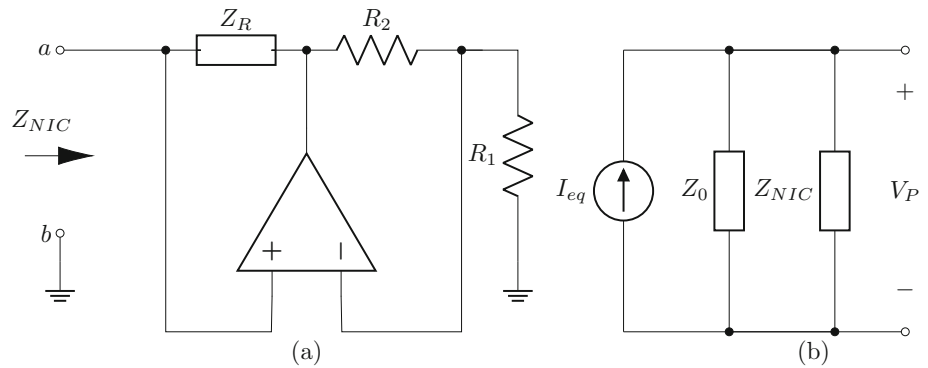
$$Z_{NIC}|_{\Im(Y)=0} = j\frac{X_p \cdot X_{C_p}}{X_p - X_{C_p}} \qquad (15)$$

In most instances, it is reasonable to assume that $X_p >> X_{C_p}$. Consequently, the NIC input impedance can be simplified as $Z_{NIC} \approx jX_{C_p}$, resulting in the impedance of a negative capacitor ($-C_P$). Indeed, if one disregards the impact of the mechanical impedance Z_m, the piezoelectric capacitance C_P can be nullified by utilizing (13) in (15). Furthermore, the matching impedances Z_{NIC} and X_{C_p} are ideally achieved irrespective of ω because they have both the same function of frequency ($f(\omega) \propto \frac{1}{\omega}$) but opposite signs in their imaginary parts.

2.2.2 SSHI

This approach implements a switched passive inductance in parallel to the output terminals of the PEH, as shown in Fig. 7. This inductance must be closed and then opened precisely at two instants in time, forcing the inversion of the voltage V_P polarity. Considering that the motion of the cantilever beam is an unidirectional harmonic sinusoidal and is such that at time $t = 0$ s, the piezoelectric capacitance C_P is charged with the voltage $V_{C_o} = V_{Rect} + 2V_D$, where V_D is the polarization voltage of the diode. The inductance L_C should be switched on when mechanical displacement of the beam u is at its maximum or $\dot{u} = 0$, according to (4).

The impedance Z_m is very large, and despite the dumping effect, its influence on the voltage V_P can be neglected. Also, because the frequency of mechanical oscillation is low, the voltage V_P remains approximately constant until the instant the inductance L_C is switched. From then on, a predominantly under-damped response from an LCR circuit with a very low resistance R_{L_C} can be observed. Figure 8a depicts the (simplified) series LCR circuit, comprising the instantaneous stored voltage in C_P, V_P, the series switched inductance and intrinsic resistance L_C and R_{L_C} respectively. This circuit can be considered separately only because the discharge of C_P and the inversion of the polarity of V_P occur very rapidly.

Thus, the under dumped voltage V_P can be calculated (disregarding the low frequency harmonically oscillations):

$$V_{P_{SSHI}}(t) = V_{C_o} e^{-\frac{R_{L_C}}{2L_C}t} \left[\cos\left(\sqrt{\frac{1}{L_C C_P} - \left(\frac{R_{L_C}}{2L_C}\right)^2} t\right) \right.$$
$$\left. + \frac{\frac{R_{L_C}}{2L_P}}{\sqrt{\frac{1}{L_C C_P} - \left(\frac{R_{L_C}}{2L_C}\right)^2}} \sin\left(\sqrt{\frac{1}{L_C C_P} - \left(\frac{R_{L_C}}{2L_C}\right)^2} t\right) \right]$$

$$(16)$$

Disregarding the second part of (16), and recognizing that $\left(\frac{R}{2L}\right)^2 << \frac{1}{LC}$, we can conclude that the first time of inversion cycle of $V_P(t)$ occurs at (Badel et al., 2006; Lefeuvre et al., 2005):

$$t_{\frac{T}{2}} = \pi\sqrt{L_C C_P} \qquad (17)$$

After inverting the voltage and charging the capacitor C_P with V_{C_o}, the switch is opened. Figure 8b shows the equivalent circuit with the capacitor charged after inversion and Fig. 9 shows the open-circuit normalized voltage and current waveforms, with SSHI. It is interesting to note that in this case, the voltage changes the sinusoidal shape due to the switch effect.

The inductance switches every mechanical half-cycle, when the current is zero (or the cantilever beam reverses the direction of displacement). The electrical inversion time is much faster ($\approx 1000\times$) than the mechanical oscillation frequency.

Figure 3 shows the dependence of the electrical domain on the speed of movement of the bar, represented by $\dot{u}$, which is reflected with the factor α. Considering an impulse type stimulus F, we have a natural response of the system, or oscillation in the fundamental mode. When the electrical impedance is reflected to the mechanical domain, the mechanical parameters M, D and K are modified. Thus the natural response of the cantilever beam is also modified as well as the phase and magnitude of $\dot{u}$. The SSHI method
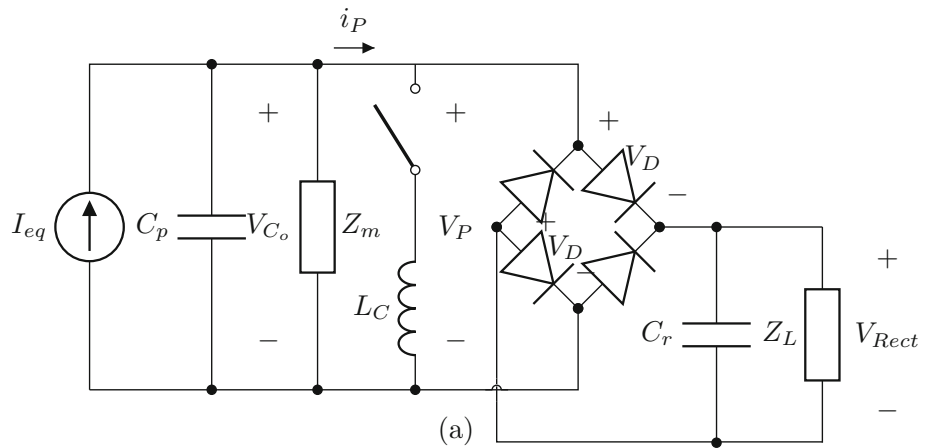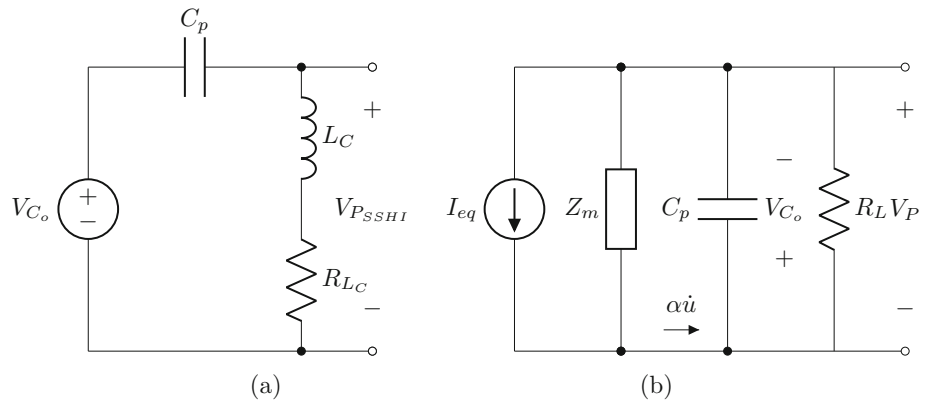
Fig. 7 PEH equivalent electrical circuit with SSHI

(a)

Fig. 8 **a** Simplified switched on inductance on SSHI equivalent electrical circuit of charged C_p and losses of a passive inductance L_C **b** equivalent PEH circuit after SSHI switched off

(a)   (b)

always detects the inversion point of u forcing V_P (no matter the waveform shape) to remain in phase with the current $\alpha\dot{u}$ as shown in Fig. 9 (when $R_L \to \infty$). The current $\alpha\dot{u}$ shown in Fig. 3 can be defined by:

$$\alpha\dot{u} = \alpha\frac{F_m}{M}e^{-\frac{(R_s+D)}{2M}t}\left[\cos\omega t - \frac{B}{2\omega}\sin\omega t\right] \quad (18)$$

where,

$$\omega = \sqrt{(k+\frac{1}{C_s})\frac{1}{M} - \frac{(R_s+D)^2}{4M^2}} \quad (19)$$

and R_s, C_s are the representation of the series resistance and capacitance reflected from the electrical domain to the mechanical domain as $Z_s = R_s - \frac{j}{\omega C_s}$.

Fig. 9 Normalized voltage V_P and current $\alpha\dot{u}$ on SSHI when $R_L \to \infty$

3 Experimental Setup and Evaluation

A mechanical structure was constructed, featuring an aluminum cantilever beam, to conduct a comparative study of compensation strategies. The piezoelectric harvester patch (Midè - V20W) was affixed to the cantilever beam, approximately at the location 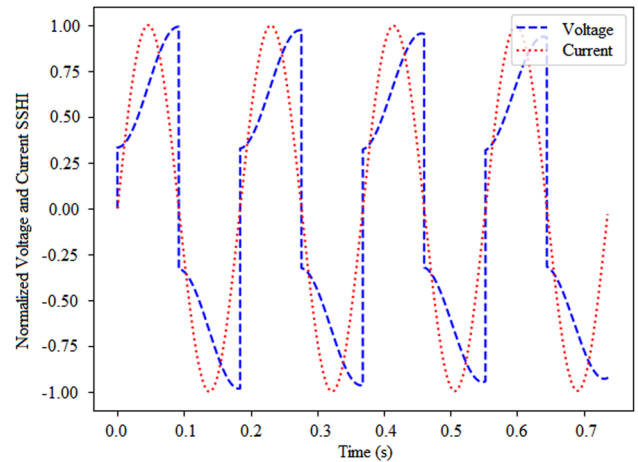of the first mode oscillation node, to drive the mechanical oscillation with an electrical stimulus. The primary properties and parameters of both the cantilever beam and the PEH are detailed in Table 1. The entire experimental setup is depicted in Fig. 10. In this arrangement, a piezoelectric actuator (Midè - QP20W) applies the mechanical stimulus, driven by a power amplifier (Midè QPA3202). The power amplifier tracks a low-power output from the sig-

Fig. 10 Experimental setup: **a** Power amplifier; **b** dSPACE Board; **c** cantilever beam; and **d** compensation circuit
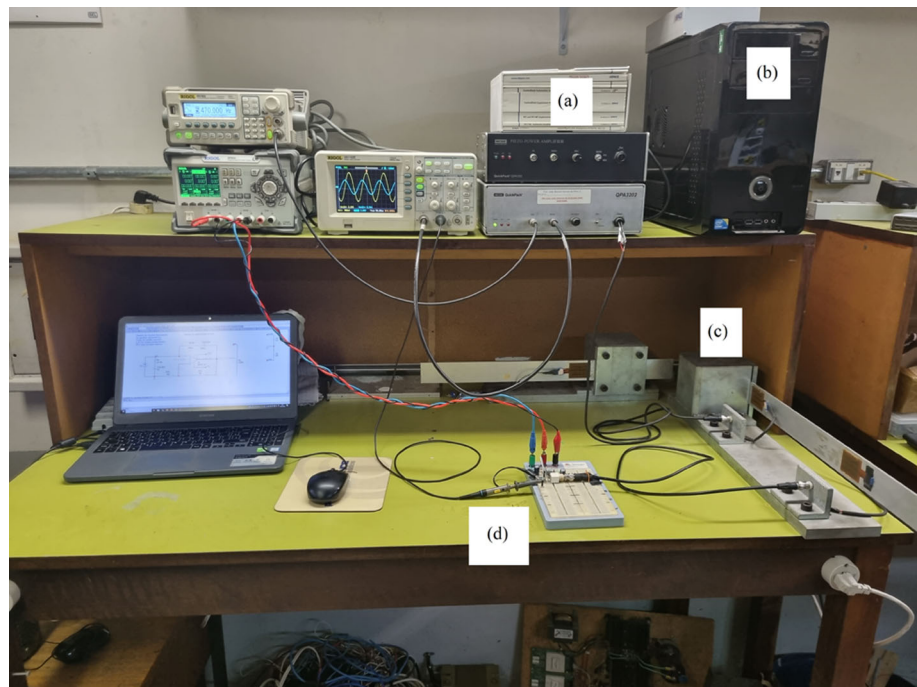

Table 1 Beam and PEH properties

Parameter	Beam	PEH	Unit
Length	710	45.97	mm
Width	50	33.02	mm
Thickness	3	0.762	mm
Young's modulus	7×10^{10}	6.7×10^{10}	N/m^2
Piezoelec. voltage const. g_{31}	—	-11.3×10^{-3}	Vm/N
Piezoelec. charge const. d_{31}	—	-190×10^{-12}	m/V
Coupling factor, k_{31}	—	0.36	—
Intrinsic capacitance C_p	—	126	nF

nal generated (or from a real-time dSpace (DS1104) board), and the entire control process can be executed on a computer.

Figure 11a shows a detailed view of the PEH attached to the cantilever beam. The PEH was attached on the position of maximum deflection in the first mode of vibration. In Fig. 11b the side view of the cantilever beam can be seen with connections between the transducers, the power amplifier and the compensation circuit. Both the piezoelectric actuator and the PEH have been attached to the cantilever beam according to the model depicted in Fig 2.

The cantilever beam was modeled and analyzed using finite element analysis software (FEM) to determine its natural frequencies (vibration modes). These findings were experimentally confirmed by sweeping a range of frequencies while monitoring the magnitudes of displacement in the experimental setup. The results are presented in Table 2 (Coelho et al., 2018). The first mode represents the free mode frequency at which the beam oscillates whenever it is driven for a short period, such as by an impulse function.

From the parameters of Table 1 and the relations defined by Lefeuvre et al. (2005), we calculate the coefficients of (5) and the results of (11), shown on Table 3. One should notice that for the natural vibration frequency of $f_n = 5.47$ Hz the reflected mechanical impedance Z_m is much higher than the capacitive reactance of the intrinsic piezoelectric capacitance C_P, which is approximately 231 kΩ. The total output impedance of the PEH at the natural vibration frequency is $Z_o = (20.25 - j283.1)$ kΩ.

Once the output impedance of the PEH is defined, it is possible to design the NIC circuit using the imaginary part of Z_o, resulting in an equivalent output capacitance of $C_o = 102.8$ nF at the natural vibration frequency f_n. The circuit of Fig. 6 has been implemented with $R_1 = R_2 = 100$ kΩ 1%, $C = 100$ nF and the micropower operational amplifier OP290.

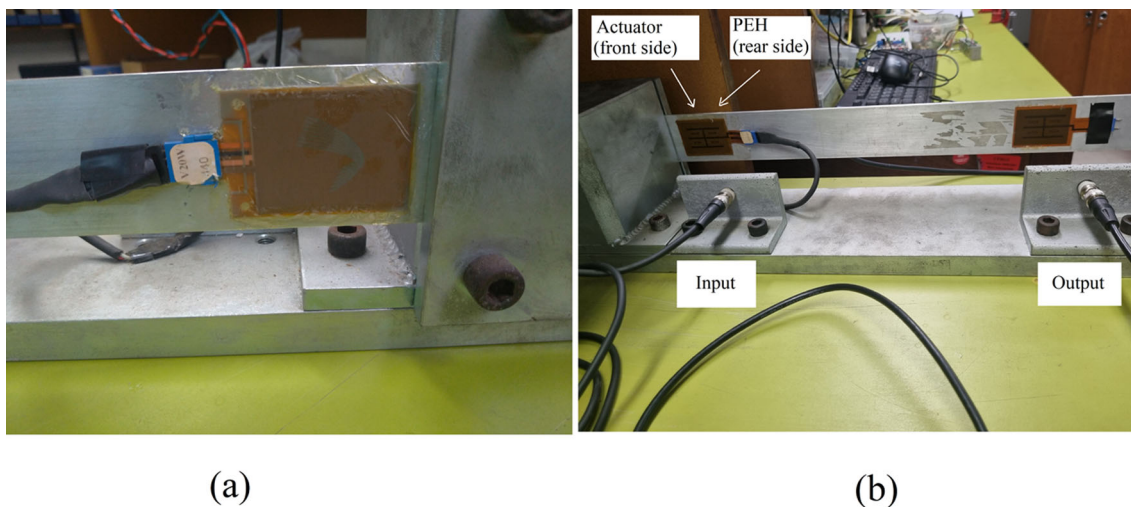(a)   (b)

Fig. 11 **a** PEH—piezoelectric energy harvester detailed view; **b** side view of the cantilever beam with transducers attached and cable connections

3.1 NIC Stability Analysis and Input Impedance Measurement

The NIC implementation is generally stable for a broad frequency range. However, external voltage or current sources with output impedances connected at the input terminals of the NIC can lead the circuit to instability because there are both negative and positive feedback working on the operational amplifier, as depicted in Fig. 12. The transfer function can be expressed by:

$$\frac{V_o}{V_i} = \frac{A_o}{1 + A_o(\beta_- - \beta_+)} \tag{20}$$

where V_i and V_o are the input and output voltage of the operational amplifier of Fig. 6, respectively. A_o is the open-loop gain of the operational amplifier, β_- is the negative feedback factor, and β_+ is the positive feedback factor.

The connection of the NIC circuit at the output terminals of the PEH allows a positive feedback factor of

$$\beta_+ = \frac{Z_o}{Z_o + Z_R} \tag{21}$$

on the other hand, (from Fig. 6) the negative feedback factor can be calculated by:

$$\beta_- = \frac{R_1}{R_1 + R_2} \tag{22}$$

In order to keep the stability, the poles of the transfer function of (20) must be located at the Laplace's domain left half-plane, then $\beta_- > \beta_+$ must be satisfied. However, the proper matching impedance requires that $Z_o = -Z_{in}$. Thus, the relation between the output impedance of the PEH, Z_o,

Table 2 Vibration mode frequencies of the cantilever beam

Vibration mode	f_{sc} [Hz][1]	f_{oc} [Hz][2]
1st	5.47	5.46
2nd	33.38	33.20
3rd	92.24	92.05
4th	177.88	177.55

[1] Short circuit frequency (f_{sc}).
[2] Open circuit frequency (f_{oc})

and the reference impedance of the NIC, Z_R, is given by:

$$Z_o = \frac{R_1}{R_2} Z_R \tag{23}$$

Using (23) in (21), one can find that $\beta_+ = \beta_-$, which eventually leads to instability when the non-ideal circuit components are present. Furthermore, certain working frequencies can drive β_+ greater than β_-, because Z_o and Z_R may have different frequency responses., that is, when (23) is not satisfied.

Figure 13 shows an RC circuit connected to the input of the NIC to measure the input impedance of the NIC circuit, preventing instabilities (Porto et al., 2023). Thus, C_{NIC} can be estimated with the difference of the input impedance obtained from measurements of I and V with and without the NIC circuit.

3.2 Power Consumption Analysis

The power consumption of the NIC circuit can be estimated considering two current components. One component is the quiescent current of the (Low Power) operational amplifier. The other is the AC signal provided by the PEH flowing

Table 3 Parameters of the mechanical constants and lumped equivalent model of the cantilever beam

Parameter	Value	Unit
D	60.244×10^{-3}	Ns/m
M	0.295	kg
K	341.748	N/m
α	0.418×10^{-3}	N/V
R	344.841	kΩ
L	1688.610	kH
C	511.2	pF
R_p	3977.233	kΩ
X_p	1225.446	kΩ
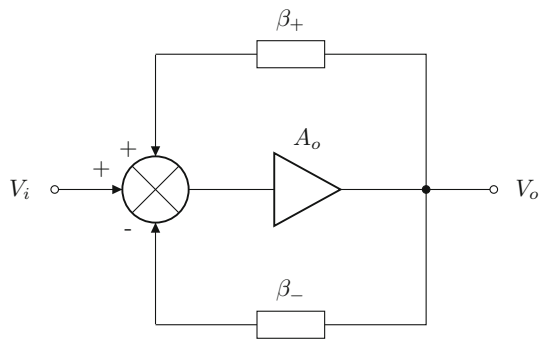
Fig. 12 NIC block diagram for feedback analysis
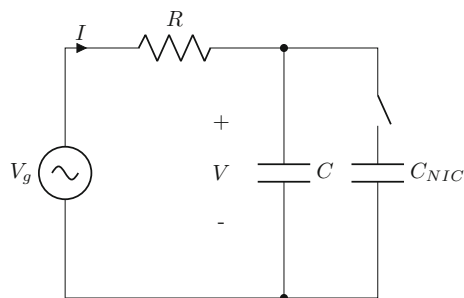
Fig. 13 Auxiliary circuit for NIC's input capacitance measurement (Porto et al., 2023)

through the passive components at the feedback loops. The total RMS current of the NIC circuit, I_S, can be estimated by:

$$I_S = \sqrt{I_{DC}^2 + I_{AC}^2} \tag{24}$$

where I_{DC} is the quiescent current of the operational amplifier and I_{AC} is the total current flowing through the passive components of the NIC block. Once determined the current I_S, which is provided by the power supply, the total power consumption of the circuit is:

$$P_C = 2 \cdot V_{cc} \cdot I_S \tag{25}$$

4 Results

4.1 AMA Results

The input impedance of the NIC has been measured for a set of five frequencies from 5.47 Hz to 100 Hz with the circuit of Fig. 13. The results are shown in Fig. 14, switching off and on the NIC circuit. The circuit without NIC yields an equivalent capacitor of 171.1 nF and with NIC, 79.6 nF. Thus, the difference of this values represents the NIC capacitance of $C_{NIC} = -91.5$ nF.

The output power of the PEH has been evaluated at the fundamental vibrating frequency f_n for a set of 10 resistive load values, as shown in Fig. 15, where the load power increases as the load increases as well up to 200 kΩ approximately. For instance, at $R_L = 220$ kΩ the output power increases 68.3% when the NIC circuit is connected.

Although Fig. 15 illustrates high load power above $R_L = 220$ kΩ, the operational amplifier saturates for $R_L > 400$ kΩ with a symmetrical power supply of 12 V. The open-circuit output voltage of the PEH is 4.5 V$_{RMS}$. Since the modulus of the PEH's output impedance is ≈ 284 kΩ, the Norton equivalent current source is ≈ 16 µA. When the NIC circuit is connected, the output impedance Z_o tends to be matched and most of the current generated by the PEH flows to the load. Considering an ideal operational amplifier connected to a symmetrical supply voltage of 12 V and matched impedances, the maximum load value would be 750 kΩ to avoid saturation at the output.

Finally, the power consumption of the NIC circuit has been evaluated according to (24) and (25). Using the operational amplifier OP290 as reference with a quiescent current of $I_{DC} = 11.3$ µA, the total AC current flowing through the passive elements Z_R, R_1 and R_2 (Fig. 6a) is 18.3 µA at $R_L = 100$ kΩ, for instance. Thus, the power consumption of the NIC circuit is ≈ 582 µW.

4.2 Generated Energy Comparison

Considering a 1 N mechanical impulse excitation at the input and a resistive load $R_L = 100$ kΩ and also considering the properties of the cantilever beam and the constants presented in the Tables 1, 2 and 3 the energy generated until approximately the extinction of the mechanical movement are shown in Fig. 16.

In an ideal system (lossless), the SSHI technique outperforms the PEH without any compensation. However, the AMA performs even better. The superior performance of the AMA is attributed to the nullification of the reactance of the capacitor C_P by the negative capacitor's reactance in parallel. In contrast, with the SSHI, the capacitor is charged during the voltage inversion (in the switching of the inductance), but its capacitive reactance is in series with the accumulated

Fig. 14 Effect of the NIC circuit on the capacitive reactance measured in a set of five frequencies (Porto et al., 2023)
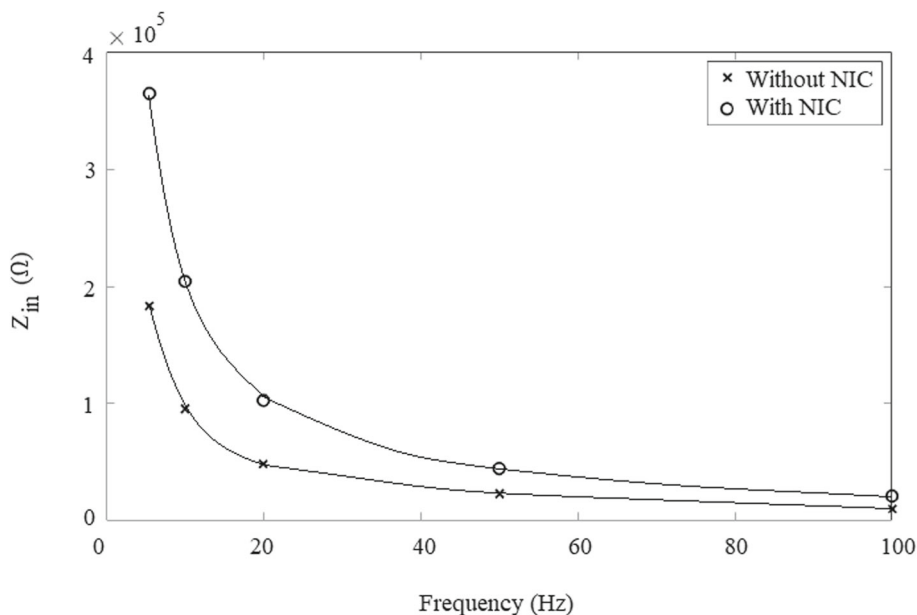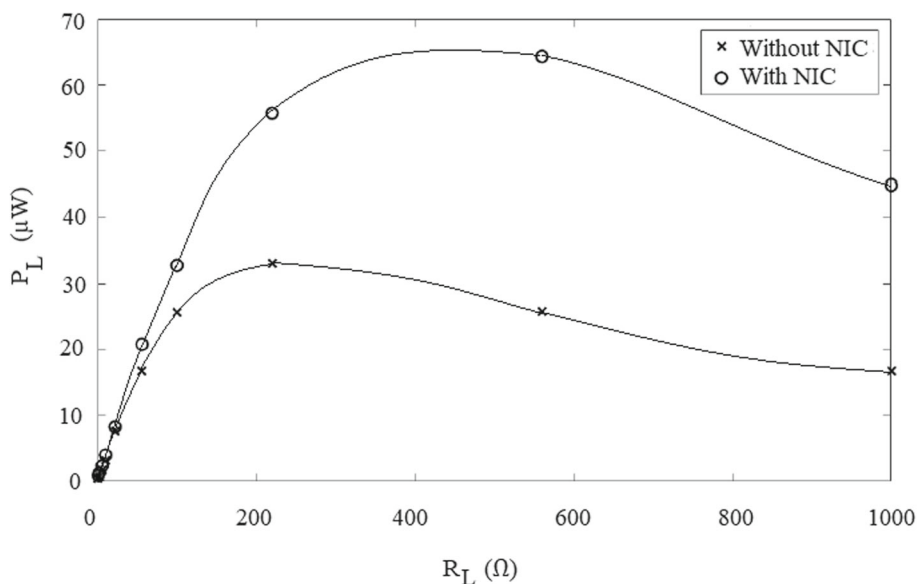

Fig. 15 Measured RMS power values at a set of resistive loads R_L (Porto et al., 2023)

electrical voltage. While the energy difference may appear small, it's noteworthy that Fig. 16 depicts only one event (a unit impulse). When considering a series of events (e.g., 100 impulses), the energy difference becomes relatively large.

Figure 16 also illustrates that, when considering a sequence of stimuli, the time interval between them impacts the difference in harvested energy. The observed energy difference stabilizes (in the presented cantilever beam) in approximately $t > 10\,\mathrm{s}$, coinciding with the period when most of the mechanical movement occurs.

Considering real systems, both SSHI and AMA compensations have certain limitations. In the case of SSHI, switching occurs when the current $\alpha \dot{u} = 0$ or when the cantilever beam's movement is at its extremes (maximum displacement). Therefore, the technique requires the presence of a current sense circuitry, along with a switch (e.g., a MOSFET) and an electronic drive circuit, all of which consume energy (E_{csshi}). For AMA, the limitations are more significant. In addition to the need to provide energy for the NIC (E_{cama}), there is also the challenge of dealing with voltage and current limits of the active component. It is crucial to ensure that the component operates within its linear region to avoid saturation. Furthermore, the AMA method depends on the oscillation frequency of the cantilever beam, unlike SSHI.

From an energy balance perspective, implementing any compensation only makes sense if the net energy gain, calculated as the energy generated with compensation E_{gc} minus
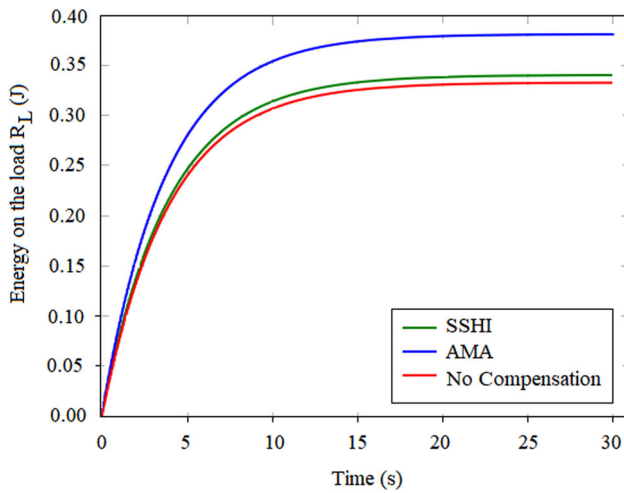
Fig. 16 Energy on $R_L = 100\,\text{k}\Omega$ after stimulus of $F = 1\,\text{N}$ (impulse) at the end of the cantilever beam until the extinction of the mechanical movement

the energy consumed by the technique's implementation, exceeds the energy generated with no compensation E_g. The energy balance equation for SSHI is as follows:

$$E_{sshi} = E_{gc} - E_{csshi} > E_g \qquad (26)$$

and for AMA:

$$E_{ama} = E_{gc} - E_{cama} > E_g. \qquad (27)$$

The energy consumption of either technique depends on the technology, and the prevailing trend is that the performance of electronic components continues to improve. For SSHI, selecting efficient active components, both for detecting switching times and activating the switch, is sufficient to optimize its performance. In the case of AMA, careful design is necessary to prevent inappropriate operating conditions while simultaneously aiming for the maximum performance of the harvester.

Figure 16 indicates that both compensation methods enhance the power at the load. The AMA results yield an energy at the load of 0.38 J. The energy required by this approach can be calculated using the power consumed by the NIC circuit (582 μW) over the 20-second interval, resulting in $E_{cama} = 0.0116\,\text{J}$. Thus, the net energy of AMA is $E_{ama} = 0.368\,\text{J}$. It is noteworthy that even if SSHI had no losses ($E_{sshi} = 0.34\,\text{J}$), the AMA compensation method would still be superior to the SSHI approach. Considering the described experiment, the energy improvement at the load is 11.5% for AMA and 3% for SSHI.

5 Conclusion

This article presents two distinct approaches to compensate for the intrinsic capacitive impedance in a Piezoelectric energy harvester system (PEH). It begins by showing the structure of a cantilever beam, providing its physical dimensions and defining the overall dynamic response, including the natural vibration modes. The PEH is affixed to the cantilever beam in a suitable position to harvest the first vibration mode. Subsequently, the electromechanical circuit of the cantilever beam with the PEH is analyzed, and the voltage response at the load is calculated.

The approaches discussed in this article are the active matching approach (AMA) and the synchronized switching on inductor (SSHI). Their effects on load power have been calculated and compared. Both approaches were initially analyzed considering ideal lossless systems with steady-state sinusoidal mechanical input and a single impulse. The calculations included electrical power and total energy in the load. Theoretical and experimental results demonstrate that the active compensation method (AMA) is more efficient than SSHI. For instance, in the presented experimental analysis, there was an 11.5% energy improvement for a single mechanical impulse in the AMA evaluation with $R_L = 100\,\text{k}\Omega$ and a 3% improvement for the SSHI method.

While the AMA compensation method shows promising results over SSHI, the energy consumed by the NIC circuit is highly dependent on the technology used. Low-power operational amplifiers are essential in this approach to enable self-powering of the compensation block. Additionally, electronic devices such as operational amplifiers pose constraints related to the PEH output voltage range and potential saturation problems. However, the design of the AMA compensation is easier than SSHI, which involves zero-crossing current sense, a comparator, and a FET-type switch. It's worth noting that SSHI has the advantage of being frequency-independent, while AMA requires tuning. Despite technological challenges, the results of AMA's energy improvement are practically four times higher than that of SSHI.

Declarations

Conflicts of interest The authors declare that they have no known competing financial interests or personal relationships that could have appeared to influence the work reported in this paper.

References

Arroyo, E., Badel, A., Formosa, F., Wu, Y., & Qiu, J. (2012). Comparison of electromagnetic and piezoelectric vibration energy harvesters: Model and experiments. *Sensors and Actuators A: Physical, 183*, 148–156. https://doi.org/10.1016/j.sna.2012.04.033

Alexander, C. K., & Sadiku, M. N. O. (2013). *Fundamentos de Circuitos Elétricos* (5th ed., p. 874). Bookman: Porto Alegre.

Batra, A. K., Currie, J. R., Alomari, A. A., Aggarwal, M. D., & Bowen, C. R. (2018). A versatile and fully instrumented test station for piezoelectric energy harvesters. *Measurement, 114*, 9–15. https://doi.org/10.1016/j.measurement.2017.08.038

Badel, A., Guyomar, D., Lefeuvre, E., & Richard, C. (2006). Piezoelectric energy harvesting using a synchronized switch technique. *Journal of Intelligent Material Systems and Structures, 17*(8–9), 831–839. https://doi.org/10.1177/1045389X06057533

Bradai, S., Naifar, S., Trigona, C., Baglio, S., & Kanoun, O. (2021). An electromagnetic/magnetoelectric transducer based on nonlinear RMSHI circuit for energy harvesting and sensing. *Measurement, 177*, 109307. https://doi.org/10.1016/j.measurement.2021.109307

Brufau-Penella, J., & Puig-Vidal, M. (2009). Piezoelectric energy harvesting improvement with complex conjugate impedance matching. *Journal of Intelligent Material Systems and Structures, 20*(5), 597–608. https://doi.org/10.1177/1045389X08096051

Bao, B., & Tang, W. (2017). Semi-active vibration control featuring a self-sensing SSDV approach. *Measurement, 104*, 192–203. https://doi.org/10.1016/j.measurement.2017.03.018

Bao, B., Wang, Q., Wu, N., & Zhou, S. (2021). Hand-held piezoelectric energy harvesting structure: Design, dynamic analysis, and experimental validation. *Measurement, 174*, 109011. https://doi.org/10.1016/j.measurement.2021.109011

Coelho, M. A. J., Flores, J. V., & Brusamarello, V. J. (2018). Evaluation of the output load effect on a piezoelectric energy harvester. *Journal of Control, Automation and Electrical Systems, 29*(4), 480–488. https://doi.org/10.1007/s40313-018-0383-x

Chao, P. C. P. (2011). Energy harvesting electronics for vibratory devices in self-powered sensors. *IEEE Sensors Journal, 11*(12), 3106–3121. https://doi.org/10.1109/JSEN.2011.2167965

Cesarini, D., Jelicic, V., Kuri, M., Marinoni, M., Brunelli, D., & Bilas, V. (2017). Experimental validation of energy harvesting-system availability improvement through battery heating. *IEEE Sensors Journal, 17*(11), 3497–3506. https://doi.org/10.1109/JSEN.2017.2691580

Deepak, P., & George, B. (2021). Piezoelectric energy harvesting from a magnetically coupled vibrational source. *IEEE Sensors Journal, 21*(3), 3831–3838. https://doi.org/10.1109/JSEN.2020.3025216

Erturk, A., & Inman, D. J. (2008). Issues in mathematical modeling of piezoelectric energy harvesters. *Smart Materials and Structures, 17*(6), 065016.

Foster, R. M. (1924). A reactance theorem. *The Bell System Technical Journal, 3*(2), 259–267. https://doi.org/10.1002/j.1538-7305.1924.tb01358.x

Franco, S. (2002). *Design with Operational Amplifiers and Analog Integrated Circuits* (2nd ed.). New York: McGraw-Hill.

Fan, S., Tang, Y., Chi, H., Hou, D., Zhang, G., & Cao, Y. (2024). A wearing orientation-independent electromagnetic self-powered sensor for human activity recognition based on biomechanical energy scavenging. *Measurement, 224*, 113926. https://doi.org/10.1016/j.measurement.2023.113926

Guyomar, D., Badel, A., Lefeuvre, E., & Richard, C. (2005). Toward energy harvesting using active materials and conversion improvement by nonlinear processing. *IEEE Transactions on Ultrasonics, Ferroelectrics, and Frequency Control, 52*(4), 584–595. https://doi.org/10.1109/TUFFC.2005.1428041

Garbuio, L., Lallart, M., Guyomar, D., Richard, C., & Audigier, D. (2009). Mechanical energy harvester with ultralow threshold rectification based on SSHI nonlinear technique. *IEEE Transactions on Industrial Electronics, 56*(4), 1048–1056. https://doi.org/10.1109/TIE.2009.2014673

Giuliano, A., & Zhu, M. (2014). A passive impedance matching interface using a PC Permalloy Coil for practically enhanced piezoelectric energy harvester performance at low frequency. *IEEE Sensors Journal, 14*(8), 2773–2781. https://doi.org/10.1109/JSEN.2014.2316091

Huang, Y.-S., & Hsieh, P.-H. (2021). Interface circuits for piezoelectric energy harvesting: A review of designs and methods. *IEEE Solid-State Circuits Magazine, 13*(4), 98–111. https://doi.org/10.1109/MSSC.2021.3111388

Halim, D., & Moheimani, S. O. R. (2001). Spatial resonant control of flexible structures: Application to a piezoelectric laminate beam. *IEEE Transactions on Control Systems Technology, 1*(1), 37–53. https://doi.org/10.1109/87.896744

Henrion, D., Prieur, C., & Tliba, S. (2004). Improving conditioning of polynomial pole placement problems with application to low-order controller design for a flexible beam. *LAAS-CNRS Research Report* **1**(04163).

IEEE (1988). IEEE standard on piezoelectricity. ANSI/IEEE Std 176-1987, 1–66 https://doi.org/10.1109/IEEESTD.1988.79638.

Kraśny, M. J., & Bowen, C. R. (2021). A system for characterisation of piezoelectric materials and associated electronics for vibration powered energy harvesting devices. *Measurement, 168*, 108285. https://doi.org/10.1016/j.measurement.2020.108285

Kuang, Y., Ruan, T., Chew, Z. J., & Zhu, M. (2017). Energy harvesting during human walking to power a wireless sensor node. *Sensors and Actuators A: Physical, 254*, 69–77. https://doi.org/10.1016/j.sna.2016.11.035

Khoo, S. Y., Radeef, Z. S., Ong, Z. C., Huang, Y.-H., Chong, W. T., & Ismail, Z. (2017). Structural dynamics effect on voltage generation from dual coupled cantilever based piezoelectric vibration energy harvester system. *Measurement, 107*, 41–52. https://doi.org/10.1016/j.measurement.2017.05.008

Kalantarian, H., & Sarrafzadeh, M. (2016). Pedometers without batteries: An energy harvesting shoe. *IEEE Sensors Journal, 16*(23), 8314–8321. https://doi.org/10.1109/JSEN.2016.2591331

Lossouarn, B., Aucejo, M., Deü, J. F., & Multon, B. (2017). Design of inductors with high inductance values for resonant piezoelectric damping. *Sensors and Actuators A: Physical, 259*(Supplement C), 68–76.

Lefeuvre, E., Badel, A., Richard, C., & Guyomar, D. (2005). Piezoelectric energy harvesting device optimization by synchronous electric charge extraction. *Journal of Intelligent Material Systems and Structures, 16*(10), 865–876. https://doi.org/10.1177/1045389X05056859

Lallart, M., Garbuio, L., Petit, L., Richard, C., & Guyomar, D. (2008). Double synchronized switch harvesting (dssh): a new energy harvesting scheme for efficient energy extraction. *IEEE Transactions on Ultrasonics, Ferroelectrics, and Frequency Control, 55*(10), 2119–2130. https://doi.org/10.1109/TUFFC.912

Liang, J., & Liao, W.-H. (2010). Energy flow in piezoelectric energy harvesting systems. *Smart Materials and Structures, 20*(1), 015005. https://doi.org/10.1088/0964-1726/20/1/015005

Liang, J., & Liao, W.-H. (2011). Energy flow in piezoelectric energy harvesting systems. *Smart Materials and Structures, 20*(1), 015005. https://doi.org/10.1088/0964-1726/20/1/015005

Liang, J., & Liao, W.-H. (2012). Impedance modeling and analysis for piezoelectric energy harvesting systems. *Mechatronics, IEEE/ASME Transactions on, 17*(6), 1145–1157. https://doi.org/10.1109/TMECH.2011.2160275

Liang, J., & Liao, W.-H. (2012). Impedance modeling and analysis for piezoelectric energy harvesting systems. *IEEE/ASME Transactions on Mechatronics, 17*(6), 1145–1157. https://doi.org/10.1109/TMECH.2011.2160275

Liu, Y., Tian, G., Wang, Y., Lin, J., Zhang, Q., & Hofmann, H. F. (2009). Active piezoelectric energy harvesting: General principle and experimental demonstration. *Journal of Intelligent Material Systems and Structures,20*(5), 575–585. https://doi.org/10.1177/1045389X08098195http://jim.sagepub.com/content/20/5/575.full.pdf+html

Lallart, M., Wu, Y. C., & Guyomar, D. (2012). Switching delay effects on nonlinear piezoelectric energy harvesting techniques. *IEEE Transactions on Industrial Electronics, 59*(1), 464–472. https://doi.org/10.1109/TIE.2011.2148675

Moheimani, R., & Fleming, A. J. (2006). *Piezoelectric transducers for vibration control and damping* Advances in industrial control (1st ed.). London: Springer. https://doi.org/10.1007/1-84628-332-9

Naifar, S., Bradai, S., Viehweger, C., & Kanoun, O. (2017). Survey of electromagnetic and magnetoelectric vibration energy harvesters for low frequency excitation. *Measurement, 106*, 251–263. https://doi.org/10.1016/j.measurement.2016.07.074

Peng, Y., Choo, K. D., Oh, S., Lee, I., Jang, T., Kim, Y., Lim, J., Blaauw, D., & Sylvester, D. (2019). An efficient piezoelectric energy harvesting interface circuit using a sense-and-set rectifier. *IEEE Journal of Solid-State Circuits, 54*(12), 3348–3361. https://doi.org/10.1109/JSSC.2019.2945262

Porto, R.W., Murliky, L., Brusamarello, V.J., & De Sousa, F.R. (2023). Non-foster circuit compensation for piezoelectric energy harvesters. In *2023 7th international symposium on instrumentation systems, circuits and transducers (INSCIT)* (pp. 1–6). https://doi.org/10.1109/INSCIT59673.2023.10258481

Priya, S. (2007). Advances in energy harvesting using low profile piezoelectric transducers. *Journal of Electroceramics, 19*(1), 167–184. https://doi.org/10.1007/s10832-007-9043-4

Pradeesh, E. L., Udhayakumar, S., Vasundhara, M. G., & Kalavathi, G. K. (2022). A review on piezoelectric energy harvesting. *Microsystem Technologies, 28*(10), 1797–1830. https://doi.org/10.1007/s00542-022-05334-4

Pan, F., Xu, Z., Jin, L., Pan, P., & Gao, X. (2017). Designed simulation and experiment of a piezoelectric energy harvesting system based on vortex induced vibration. *IEEE Transactions on Industry Applications*. https://doi.org/10.1109/TIA.2017.2687401

Qi, L., Pan, H., Pan, Y., Luo, D., Yan, J., & Zhang, Z. (2022). Aa review of vibration energy harvesting in rail transportation field. *IScience, 25*(3), 1–30. https://doi.org/10.1016/j.isci.2022.103849

Roy, S., Azad, A. N. M. W., Baidya, S., Alam, M. K., & Khan, F. (2022). Powering solutions for biomedical sensors and implants inside the human body: A comprehensive review on energy harvesting units, energy storage, and wireless power transfer techniques. *IEEE Transactions on Power Electronics, 37*(10), 12237–12263. https://doi.org/10.1109/TPEL.2022.3164890

Ruan, T., Chew, Z. J., & Zhu, M. (2017). Energy-aware approaches for energy harvesting powered wireless sensor nodes. *IEEE Sensors Journal, 17*(7), 2165–2173. https://doi.org/10.1109/JSEN.2017.2665680

Shu, Y. C., & Lien, I. C. (2006). Analysis of power output for piezoelectric energy harvesting systems. *Smart Materials and Structures, 15*(6), 1499.

Shen, H., Qiu, J., Ji, H., Zhu, K., & Balsi, M. (2010). Enhanced synchronized switch harvesting: a new energy harvesting scheme for efficient energy extraction. *Smart Materials and Structures, 19*(11), 115017. https://doi.org/10.1088/0964-1726/19/11/115017

Steigerwald, R. L. (1988). A comparison of half-bridge resonant converter topologies. *IEEE Transactions on Power Electronics, 3*(2), 174–182. https://doi.org/10.1109/63.4347

Varoto, P. S. (2015). Issues in experimental testing of piezoelectric energy harvesters. In A. Wicks (Ed.), *Shock & vibration, aircraft/aerospace, and energy harvesting* (Vol. 9, pp. 11–17). Cham: Springer.

Wu, W. J., Wickenheiser, A. M., Reissman, T., & Garcia, E. (2009). Modeling and experimental verification of synchronized discharging techniques for boosting power harvesting from piezoelectric transducers. *Smart Materials and Structures, 18*(5), 055012. https://doi.org/10.1088/0964-1726/18/5/055012

Xu, Y., Bader, S., & Oelmann, B. (2018). A survey on variable reluctance energy harvesters in low-speed rotating applications. *IEEE Sensors Journal, 18*(8), 3426–3435. https://doi.org/10.1109/JSEN.2018.2808377

Xia, H., Xia, Y., Ye, Y., Qian, L., Shi, G., & Chen, R. (2018). Analysis and simulation of synchronous electric charge partial extraction technique for efficient piezoelectric energy harvesting. *IEEE Sensors Journal, 18*(15), 6235–6244. https://doi.org/10.1109/JSEN.2018.2846256